ACS Photonics

Letter

pubs.acs.org/journal/apchd5

Exceptional Terahertz Wave Modulation in Graphene Enhanced by Frequency Selective Surfaces

Rusen Yan,*[,†,‡] Sara Arezoomandan,[§] Berardi Sensale-Rodriguez,*[,§] and Huili Grace Xing*[,†,‡,∥]

[†]School of Electrical and Computer Engineering and [∥]Department of Materials Science and Engineering, Cornell University, Ithaca, New York 14850, United States

[‡]Department of Electrical Engineering, University of Notre Dame, Notre Dame, Indiana 46556, United States

[§]Department of Electrical and Computer Engineering, The University of Utah, Salt Lake City, Utah 84112, United States

Supporting Information

ABSTRACT: In this paper we theoretically and experimentally analyze the design trade-offs in terahertz metamaterial modulators consisting of hybrid graphene/metal stacked structures. In these devices graphene is used as the active medium, whereas a passive metallic frequency selective surface is employed to enhance the light−matter interaction in graphene. When altering the key geometrical structural parameters, we observe a close match between our experiments and theory, showing that it is possible to achieve an optimal trade-off between modulation depth, insertion loss, and speed in these devices. Moreover, a transmission line based compact mathematical model is introduced in order to explain our experimental observations and predict the performance limits in these structures.

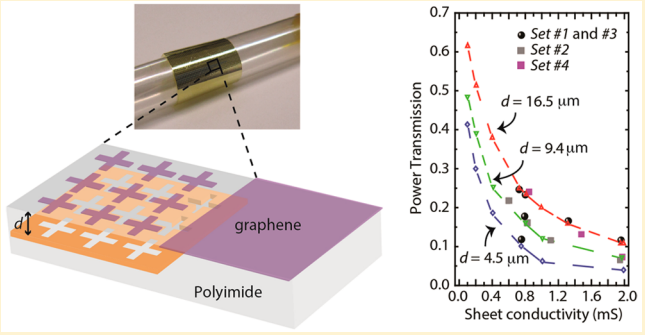

KEYWORDS: *graphene, terahertz, flexible, metamaterials, transmission line model, light−matter interaction*

The past decade has witnessed rapidly growing interest in developing devices based on two-dimensional semiconductor materials, in particular graphene.[1−4] Due to its unique electronic, optical, and mechanical properties, superior thermal properties, as well as recent developments on high-quality, large-area film growth,[5−7] graphene has emerged as an attractive material for a number of technologies such as displays, sensors, supercapacitors, water desalination, and even DNA sequencing.[8−10] In the field of terahertz (THz) research, graphene is drawing substantial attention due to its potential as the active material in emitters, detectors, and modulators.[11−13] THz technology, one of the last frontiers in the electromagnetic spectrum, holds promise in many areas, such as quality control, astronomy, sensing, and security, thus attracting a rising number of researchers to this field during the past decades.[14] However, the limited performance of THz devices reported to date restricts the development of many THz applications. One of the critically demanded improvements is in the area of THz modulators, where simultaneous high modulation depth (MD), defined as $(T_{max} - T_{min})/T_{max}$ with a maximum value of 1, where T_{max} and T_{min} represent the maximum and minimum power transmittances, respectively, through the structure within the reconfigurable range, and low insertion loss (IL), defined as $1 - T_{max}$, are required for realizing applications in THz communications, imaging, power stabilization of THz sources, and so forth. Various strategies have been proposed to tackle this challenge, including electrically or optically driven modulation based on compound semiconductors and/or metamaterial structures,[15,16] thermal modulation in semiconductors or metal oxides,[17] magnetic tuning,[18] MEMS-based geometry modulation,[19] etc.

Recently, a series of THz modulators based on graphene have been proposed and demonstrated with promising performances.[20−26] Essentially, THz transmission or reflection can be tuned by controlling the Fermi level in graphene, thus the density of states available for intraband transition induced absorption.[27] However, the superior carrier transport observed in micro- or nanometer-scale graphene cannot be readily transferred to millimeter or larger scale graphene. As a result, modulator designers turn to strategies for enhancing the light−matter interactions between graphene and THz waves by implementing resonant structures such as Fabry−Perot cavities or metamaterials.[20−23,26,28] Recently, hybrid THz modulators following this scheme have exhibited 60% transmission modulation, 2.5 dB insertion loss, and operating speed in excess of 40 MHz, where modulation is achieved through varying the resonance of localized surface plasmons in graphene.[23] Among all of these previous reports, one critical design factor that has not been widely studied is the possibility of controlling the electromagnetic field enhancement at the

Received: November 8, 2015
Published: February 11, 2016

DOI: 10.1021/acsphotonics.5b00639
ACS Photonics 2016, 3, 315−323

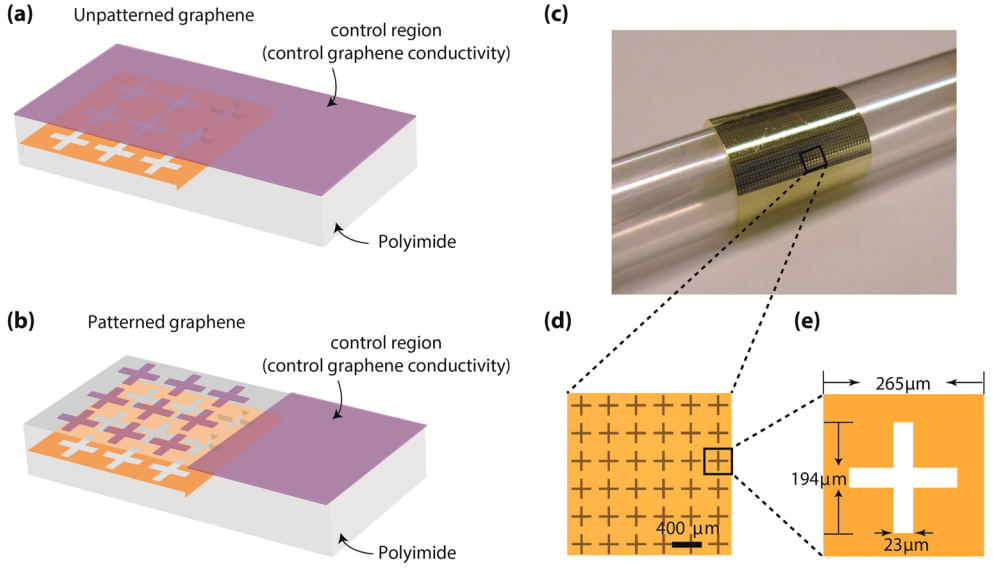

Figure 1. Analyzed metamaterial structures. (a and b) Schematic of the analyzed device structures consisting of a metallic FSS embedded in a polyimide (PI) film with nonpatterned and patterned graphene layers on top. The right half of the sample (control region), which contains unpatterned graphene on top of PI, is used to monitor the conductivity of graphene. (c) Optical image of a fabricated THz modulator on a flexible PI substrate rolled on a glass pipet. (d) Optical image showing detail of the FSS structure. (e) Sketch showing the dimensions of the FSS unit cell.

graphene plane. Graphene metamaterials typically consist of a passive metallic frequency selective surface (FSS) and one or multiple layers of graphene. In these structures the field enhancement can be controlled via placement of graphene from the plane of the FSS. For a given graphene conductivity swing range, the higher the electric field enhancement in the plane of graphene, the higher the MD due to an enhanced sensitivity of THz transmission to graphene conductivity; however, this is often accompanied by a higher IL. Therefore, there exists a trade-off between MD and IL, which needs to be considered when designing graphene-based THz modulators. This trade-off was pointed out in our earlier theoretical work.[20] However, a comprehensive study on the geometry dependence of these trade-offs and an experimental demonstration of the underlying physical principles behind optimal performance are still lacking. In this paper we present the first experimental validation of this device optimization concept proposal by using graphene as an active cross FSS (i.e., conductivity-tunable graphene FSS).

Our proof-of-principle samples for this new type of stacked hybrid THz modulators have been fabricated using graphene layers, which are separated by a polyimide (PI) spacer from a passive metallic FSS; the entire hybrid stack lies on a PI substrate. By placing the conductivity-tunable graphene layers at various separations from the FSS, (a) we are able to augment the strength of the interaction between the THz waves and graphene, which is equivalent to enhancing the effective conductivity of graphene. More importantly, we also show that (b) due to the superior ability of confining electromagnetic waves into subwavelength volumes by the metallic FSS, the graphene area (active area) required to obtain a given modulation performance can be significantly reduced. The immediate advantage of this area reduction will be an improved operation speed in voltage-actuated modulator designs because of the smaller capacitance, and thus *RC* time constant, in the device. To quantitatively model and predict the behavior of the proposed modulators based on a hybrid graphene/FSS stack, we also (c) discuss a simple transmission line model (TLM), which lets us predict the performance limits in these structures. In summary, our results indicate that our proposed modulator designs can highly augment the light−matter interaction in graphene by localizing the electric field close to the metasurface, leading to higher modulation depth, lower insertion loss, and faster speed when compared to previously reported unoptimized graphene-based THz metamaterial modulator designs. Furthermore, the proposed device design strategy provides great flexibility since it could be readily applied to other material systems by means of modifying the geometry of the total stack so as to achieve the optimal performance in each materials system.

RESULTS AND DISCUSSION

For a comprehensive study, we prepared four sets of samples, consisting of (set #1) unpatterned-graphene/PI/FSS, where the graphene conductivity was varied by means of stacking different numbers of graphene layers; (set #2) unpatterned single-layer graphene/PI/FSS, where the graphene conductivity was varied by means of chemical doping; (set #3) unpatterned single-layer graphene/PI/FSS with varying PI spacer thickness; and (set #4) patterned-graphene/PI/FSS, where the graphene conductivity was varied by means of stacking different numbers of graphene layers. The fabricated sample structures are schematically depicted in Figure 1a for the sample sets with unpatterned graphene and in Figure 1b for the sample sets with patterned graphene. All sets consist of a 100 nm thick aluminum FSS lying on a PI substrate and contain varied layers (1−3 layers) of monolayer graphene. To circumvent high IL originating from a strong local electric field, the graphene layers are separated from the FSS by a variable-thickness PI spacer layer. The distance between the FSS and the graphene layers is labeled as *d*. The fabrication process starts with a PI (PI-2600) coating (~2 μm thick) and two-step curing process on top of a bare Si substrate, followed by photolithography and 100 nm aluminum deposition to form the metallic FSS. Afterward, a second layer of PI is spin-coated to act as spacer. By varying the spin speed and using multiple spin-coating steps, various thicknesses of the PI spacer are obtained. Single-layer graphene films are grown

DOI: 10.1021/acsphotonics.5b00639
ACS Photonics 2016, 3, 315−323

using chemical vapor deposition (CVD), by Bluestone (monolayer percentage >95%), and are then transferred onto the PI/Al-FSS/PI/Si wafers using PMMA and wet etch methods.[5] For patterned graphene samples, photolithography and oxygen plasma etching are further used to define the graphene pattern geometry. Finally, the fabricated sample is peeled off from the Si substrate, forming a flexible, free-standing, and ultrathin film. Multiple layers of graphene used in this work are obtained by repeating the wet transfer process of monolayer graphene. Images of an example sample rolled on a glass pipet and a microscopic detail of the sample, respectively, are shown in Figure 1c and d. The dimensions of the cross-slot FSS are depicted in the unit-cell detail shown in Figure 1e. To account for the process-induced variations in the graphene conductivity and to improve the accuracy when comparing our experimental results with simulations and theory, each test sample contains three regions: (i) a test region, consisting of FSS/PI/graphene, (ii) a control region, consisting of PI/graphene only without FSS, as depicted in Figure 1a,b, and (iii) a reference region, consisting of PI alone. Note that all the shown transmission values through the test and control regions are normalized to the transmission through the corresponding reference PI region for each sample. The graphene conductivity in each test sample is directly measured on the control region of the sample. It is worth noting that when multiple layers of graphene are used, in order to systematically vary the graphene conductivity, all graphene layers are cut from the same piece of single-layer CVD graphene and processed at the same time.

The conductivity of graphene on each sample is experimentally determined by fitting the THz transmission spectrum through the control region and using a Drude model for the graphene sheet conductivity:[29]

$$T = \left| \frac{1}{1 + Z_0\sigma_{dc}/(1 + n_{sub})(1 + \omega^2\tau^2)} \right|^2 \quad (1)$$

where T is the measured power transmissions through the control region normalized to the transmission through a reference PI stack (without graphene or FSS), $Z_0 = 377\ \Omega$ is the vacuum impedance, $n_{sub} = 1.7$ is the refractive index of PI, and ω is the angular frequency of the THz beam. The carrier lifetime τ and the sheet conductivity σ_{dc} of the total graphene stack (one, two, or three layers) are unknown, thus set as fitting parameters. The THz spectra are measured at room temperature (RT) using a commercial THz time-domain spectroscopy system (Menlo THz-TDS) with ∼1.2 GHz resolution, beam size of ∼1 mm, and 80 dB signal-to-noise ratio. Simulations are conducted employing a high-frequency structure simulator (ANSYS HFSS) by considering graphene as a zero-thickness graphitic layer (layered impedance) with the sheet conductivity set to the experimentally determined values; results using a finite thickness[20] match those obtained employing the layered impedance model in this work. Simulations were performed for all the explored design space (in terms of spacer thickness and sheet conductivity) in order to study the effect of relaxation time. For this purpose graphene was modeled employing a Drude model. Our results, which are depicted in the Supporting Information (Figure S3), show that for small values of τ, i.e., when $\omega\tau < 1$ at resonance, the transmission spectrum is almost independent of τ (i.e., using $\tau = 0$ or $\tau = 150$ fs produces roughly the same spectra). Therefore, neglecting the effect of relaxation time and assuming the graphene optical conductivity to be purely real is a good approximation since $\tau < 50$ fs in our samples (see Figure S1).

To illustrate the effect of stacking multiple graphene layers, we performed THz spectroscopy through the control region (without FSS) of sample set #1 by varying the number of graphene layers. The fitted σ_{dc} values obtained were 0.73 ± 0.08, 1.32 ± 0.07, and 1.98 ± 0.1 mS for one, two, and three layers of graphene. This confirms that the graphene conductivity indeed roughly follows a linear trend: $\sigma_{dc} = N\sigma_0$, where N is the number of transferred graphene monolayers with a sheet conductivity of σ_0 per layer.[29] Since these results were measured in the 0.3−0.9 THz frequency range (due to the working bandwidth of our TDS system), we observed a flat transmission. In order to extract τ, we performed THz continuous wave (CW) and Fourier transform infrared spectroscopy (FTIR) measurements; typical results are depicted in the Supporting Information (Figure S1). A carrier lifetime on the order of 30−50 fs is extracted in our graphene samples, which is similar to values obtained on CVD-grown graphene by other groups.[29,30] Throughout this work, the conductivity of graphene layers in each sample has been individually monitored by employing the above-mentioned method; these values are subsequently used in our modeling section. The measured and simulated THz power transmission spectra for the graphene/FSS hybrid structures with one, two, and three layers of graphene (sample set #1) are shown in Figure 2a,b, respectively. The thickness of the spacer between the graphene layers and the FSS is kept at $d = 16.5$ μm, which ensures the same electric field strength with an identical enhancement factor at the graphene plane. The geometry and dimensions of the FSS determine the shape of center-band transmission, which in this case holds a resonance at around 0.5 THz and an intrinsic peak power transmission that can be as high as 85% (simulated) (∼15% absorption by the metal).[31] On the other hand, the total conductivity of the modulation medium (graphene) sets the transmission magnitude over the entire spectrum. In our experiments the intrinsic peak power transmission through FSS is measured to be ∼80% (for $d = 16.5$ μm) to 85% (for $d = 4.5$ μm). For the case pictured in Figure 2, which corresponds to $d = 16.5$ μm, it is remarkable that the presence of only one layer of graphene can reduce the maximum transmission from 80% to 25%, corresponding to a fractional variation of (80 − 25)/80 = 69%. With increasing graphene conductivity (by means of adding more graphene layers), the THz transmission is further reduced from 25% to 17% (two-layer graphene) and then to 12% (three-layer graphene). The reduction in transmission is attributed to boosted absorption by graphene, which can reach a maximum of 50% of the incoming power, as well as increasing reflection (∼50% at the absorption maximum) from the sample.[20,32] In this case, when the graphene sheet conductivity is varied by three times, i.e., from that in one-layer graphene to that in three-layer graphene, the fractional decrease in the transmitted power is more than 50%, i.e., (25 − 12)/25 = 52%. The above observed high-conductivity-induced low transmission phenomenon is consistent with what has been reported in previous work.[11,25,26] Again, note that the total conductivity is the sum of the conductivities of the individual graphene layers, which is not surprising considering the fact that the thickness of the overall graphene stacks (less than 2 nm) is negligible compared to the wavelength of the incident THz waves.[29] Our numerical simulations of transmission, employing the sheet conductivity

DOI: 10.1021/acsphotonics.5b00639
ACS Photonics 2016, 3, 315−323

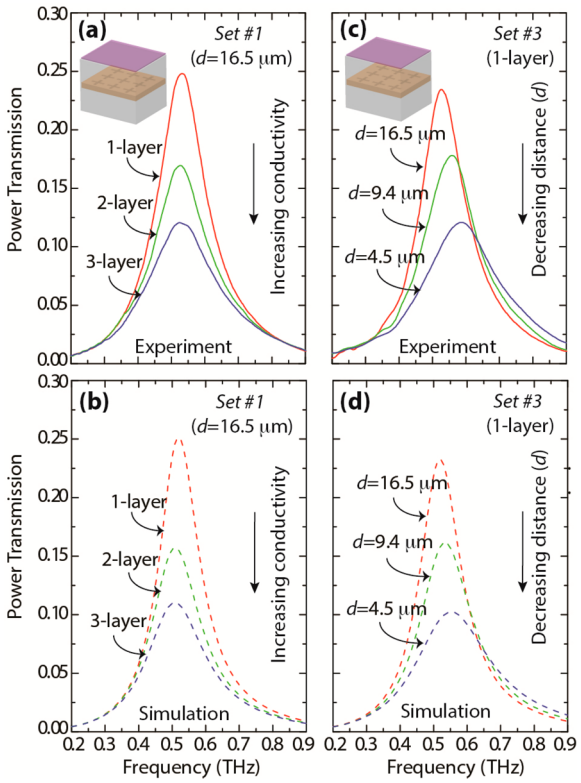

Figure 2. Measured THz transmission spectra when changing the graphene conductivity and PI spacer thickness. (a and b) Experimentally measured (a) and simulated (b) intensity transmission spectra for devices containing one, two, and three layers of graphene (sample set #1) and d = 16.5 μm. (c and d) Experimentally measured (c) and simulated (d) intensity transmission spectra for devices with one layer of graphene and various PI spacer thicknesses, d = 16.5, 9.4, and 4.5 μm, respectively (sample set #3).

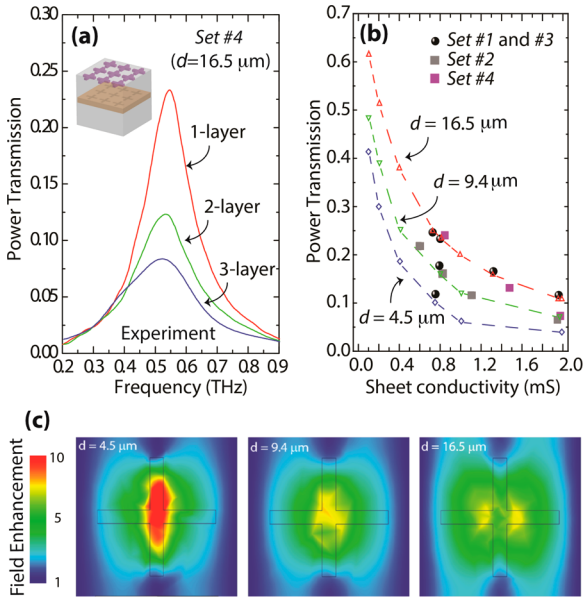

Figure 3. Terahertz transmission through devices made of patterned graphene, summary of all results, and illustration of electric field enhancement. (a) Measured power transmission spectra for devices with one, two, and three layers of patterned graphene (sample set #4). The graphene layers have been patterned to the complementary structure of that of the metallic FSS underneath. (b) Summary of the measured and simulated THz transmission (at resonance) as a function of graphene sheet conductivity for all the analyzed sample sets. The measured (solid symbols defining dashed traces) and simulated (hollow symbols) THz power transmission values are plotted for three different thicknesses of the dielectric spacer (d = 16.5, 9.4, and 4.5 μm, respectively). The black solid circles represent experimental results obtained by stacking one, two, and three graphene layers (sample set #1 and sample set #3), whereas the gray solid squares represent results for devices containing single-layer graphene where the conductivity was tuned by means of chemical doping by HNO_3 (sample set #2). The purple squares represent measurements on samples with patterned graphene (sample set #4). (c) Simulated electric filed enhancement distribution inside the plane of the graphene for different values of d. It could be clearly seen that enhancement gets smaller when graphene gets farther away from the FSS plane, which is consistent with the decrease of fitting parameter α_1 as d is increased.

values measured in the control region for each sample, exhibit an excellent agreement with the experimental results.

We also studied samples where the graphene conductivity was varied through chemical doping (sample set #2). Since HNO_3 is well known to be a p-type dopant for graphitic materials such as carbon nanotubes and graphene,[33,34] in this work the chemical doping was realized by immersing a single-layer graphene covered sample (d = 9.4 μm) in a HNO_3 solution (63 wt %) for 1−5 min, followed by a drying and baking step at 85 °C. A series of THz transmission spectra (Figure S4) through the test and control regions of the sample were measured before chemical immersion ($\sigma_{dc} \approx 0.65$ mS), immediately after doping ($\sigma_{dc} \approx 1.96$ mS), after 12 h in air ($\sigma_{dc} \approx 1.10$ mS), and after 24 h ($\sigma_{dc} \approx 0.81$ mS) in air. The decrease of sheet conductivity is a result of the dedoping process in air, that is, the removal of physically adsorbed HNO_3 molecules on the graphene surface.[34] The measured THz transmission through the test region of the samples at resonance is plotted in Figure 3b (gray squares). Similar behavior is observed when the graphene conductivity is increased due to chemical doping; in both cases the THz transmission drops as the overall graphene conductivity increases. The dashed curves with hollow symbols in Figure 3b represent the simulated peak THz transmission as a function of the graphene sheet conductivity, and each of these curves is associated with structures having different values of d. The values of measured transmission at resonance for this chemically doped sample (gray squares) in Figure 3b show good consistency with the simulations (dotted curves) as well as with our measurements on multilayer-graphene samples (black circles). This also helps confirm that stacking of multiple graphene layers behaves similarly to doping of a single layer of graphene in terms of electromagnetic wave transmission.

Beyond this, for the first time with experiments we systematically investigated the impact of the distance between the graphene layers and the FSS on the THz transmission through the structure.[20] In Figure 2c and d, measured and simulated THz transmission through three samples (sample set #3), all with single-layer graphene, but with different spacer thickness d = 16.5, 9.4, and 4.5 μm, is shown. As the graphene layer is placed closer to the FSS, the THz transmission declines from 23% to 12% and the resonance frequency blue-shifts from 0.53 to 0.58 THz, even though the graphene conductivity was maintained constant; that is, the extracted sheet conductivity from the control region was the same, in all three samples. This transmission reduction is clear evidence that the interaction between the FSS and graphene strongly depends on the

DOI: 10.1021/acsphotonics.5b00639
ACS Photonics 2016, 3, 315−323

separation distance between them. The light−matter interaction is enhanced when graphene is closer to the FSS, leading to lower transmission, as expected by our previous theory.[20] In Figure 3c we show the electric field intensity distribution at the graphene plane when the metallic FSS is placed at different distances above it; it can be clearly noticed that the electric field is greatly augmented in a region within tens of micrometers away from the FSS. It is compelling to acquire this source of control for the interaction strength by changing the location of the modulation medium. This location can be strategically chosen to realize high MD with simultaneous low IL based on the conductivity swing ranges of specific materials, i.e., not only limited to graphene. The observed frequency blue-shift of the resonance peak is primarily due to the varied sample total thickness t ($t \approx d + t_{sub}$), therefore different effective dielectric environment, where t_{sub} is the thickness of the PI substrate, which is kept as 2.2 μm in all three analyzed samples. Considering the fact that the electric field enhancement near the FSS can reach regions as far as tens of micrometers in the z-direction, a change in PI thickness can indeed translate into a different effective dielectric environment. Thinner samples could be modeled with a lower effective dielectric constant, thus higher resonant frequency (ω_r), which will be discussed in more detail in the modeling section.

One critical challenge in reported voltage-actuated graphene-based THz wave modulators is their low operation speed, which is severely limited by the large area of the employed modulation medium as well as the large THz beam size.[25,35] Integration with an FSS, as in our proposed design, could potentially tackle this problem by reducing the active area of the device (area occupied by graphene). In the near field, the electric field is highly confined at the openings of the FSS, while negligible elsewhere. As a result, we expect that the device active area (graphene) can be reduced to the FSS openings only, which effectively form a complementary pattern to that of the FSS. To demonstrate this principle, we fabricated samples with patterned graphene structures, as shown in Figure 1b. The graphene layers were patterned using oxygen plasma to a geometry consisting of the complementary structure to the underlying FSS. Photolithography was employed to define the graphene pattern, which was aligned directly on top of the openings of the metallic FSS. The measured THz transmission for samples with one, two, and three layers of graphene and d = 16.5 μm (sample set #4) is shown in Figure 3a. Similar to what was previously discussed in samples containing unpatterned graphene, a peak THz transmission ranging from 24% to 8% is observed when the total graphene sheet conductivity is varied from 0.8 to 2 mS. However, the total graphene area in these samples is reduced by around 90%. It is noted that the fractional decrease of the transmitted power slightly increased from 52% to $(24 - 8)/24 = 66\%$ after the graphene layers were patterned, which is partially caused by a higher conductivity in our patterned samples. Compared to previous reports on graphene-based THz modulators,[20,21,25,36−38] this work is the first experimental demonstration of the intrinsic geometrical design trade-offs in graphene/FSS hybrid modulator systems. Therefore, the observations here in this report can lead to practical advantages such as a higher MD, lower IL, and faster operation speed.

We could estimate the potential operation speed of an electrically actuated hybrid device structure enabled by self-gated graphene sheets separated by a 100 nm SiO_2 (or other dielectrics such as SiN_x, PMMA) dielectric as proposed and discussed in ref 20, which is primarily limited by the RC time constant ($R_{grapene}C_{ox}$) in this device structure. If the THz beam size is 1 × 1 mm^2, the number of FSS units that are needed to control the light is $N = 1^2/0.265^2$, with 0.265 mm being the FSS unit dimension. The capacitance associated with this geometry is $C_{ox} = \epsilon_r\epsilon_0 A/t_0$, where $\epsilon_r = 3.9$ and $\epsilon_0 = 8.85 \times 10^{-12}$ F/m are the relative permittivity of SiO_2 and the vacuum permittivity, respectively, and $A = NA_{FSS}$ is the total area occupied by active graphene. If the metal contacts are made to all the edges of graphene cross-slots, the resistance ($R_{graphene}$) could be estimated by $1/\sigma_{graphene}W/L \approx 60\ \Omega$ for $\sigma_{graphene}$ = 2 mS. This resistance could be further reduced by doping, but this can degrade the trade-offs with insertion loss as well as modulation depth. Therefore, the operation speed is given as $1/2\pi R_{graphene}C_{ox} \approx 0.3$ GHz, which is boosted by a factor of $\frac{L}{W}\frac{A_{beam}}{A} \approx 70$ times when compared to the case of devices consisting of unpatterned graphene. The contact resistance R_c between metal and graphene is estimated to be 4 Ω assuming a specific R_c = 100 Ω-μm and a graphene cross stripe width W = 23 μm, which is small compared to the resistance of the graphene stripe itself (∼60 Ω) and thus negligible in the operation speed estimation.[39] In Figure 3b, all the measured transmission values (solid symbols) at resonance as a function of sheet conductivity, together with simulation results (open symbols), are summarized. Instructively, both the graphene conductivity and the distance d between the FSS and the graphene layers determine the THz transmission. The graphene conductivity affects the transmission because of intraband absorption, but d also affects the transmission through modifying the strength of light−matter interaction in graphene. The first parameter, graphene conductivity, can provide active modulation, whereas the latter, d, could be chosen to achieve the best trade-off between MD and IL for specific material systems based on their conductivity swing ranges.

To gain more insight as well as to find a straightforward way to predict device performance, we discuss a simple transmission-line model to describe the behavior of the tested samples.[30,40] The employed model and analysis is similar to that discussed by Valmorra et al.[22] with its lumped-element circuit representation sketched in Figure 4a. The addition of graphene is depicted by a parallel impedance $1/\sigma_{graphene}$. The inductance induced by graphene could be ignored since for the analyzed structure and range of frequencies (see Figure S3) its contribution is quite small compared to that of the real part of conductivity ($i\omega\epsilon_0 t_{graphene} \ll \sigma_{graphene}$).[41] First, the THz transmission through the FSS embedded in a PI film with d = 16.5 μm, before graphene is transferred on top (i.e., when $\sigma_{graphene} = 0$), is measured, and these data are depicted as open circles in Figure 4b. The measured transmission could be well fitted (solid line in Figure 4b) employing the following formula:[40]

$$T = \left|\frac{2Z_{in}}{Z_{in} + Z_0}\right|^2 = \left|\frac{2}{2 + j\omega CZ_0 + Z_0/(j\omega L + R)}\right|^2 \quad (2)$$

where R, L, and C are fitting parameters corresponding to the FSS behaving as a bandpass filter. The best fitting result gives R = 0.93 Ω, L = 10.8 pH, and C = 8.6 fF. Second, two parameters, α_1 and α_2, are introduced. α_1 depicts the electric-field enhancement factor at the graphene plane, which is translated into a graphene conductivity enhancement factor in the transmission-line model. α_2 depicts the change in capacitance

DOI: 10.1021/acsphotonics.5b00639
ACS Photonics 2016, 3, 315−323

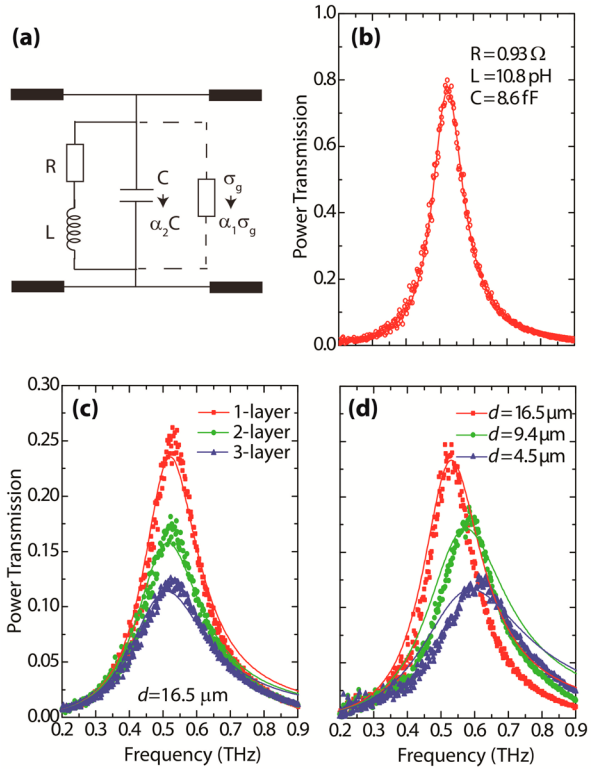

Figure 4. Transmission line model and fitting of experimental results to the model. (a) Schematic depicting the proposed transmission line model of our graphene THz modulators. Addition of the graphene layers is represented via inclusion of a parallel impedance element with sheet conductivity of σ_g to the original equivalent circuit RLC model of the FSS. Due to the near-field enhancement, the effective sheet conductivity of graphene is enhanced to $\sigma_g' = \alpha_1\sigma_g$ where α_1 (>1) represents a nonlinear enhancement factor induced by the FSS. Besides, the parameter α_2 models the variation in the structure effective capacitance due to PI thickness variations. (b) Measured (hollow dots) and fitted (solid line) transmission spectra for a sample containing the FSS alone without any graphene on top; the measured sample has a total PI thickness of 18.7 μm consisting of a PI layer of d = 16.5 μm on top of the FSS and a PI substrate of thickness 2.2 μm below the FSS. (c and d) Modeling fitting (solid lines) and measured (solid points) power transmission spectra for the samples whose measurements are shown in Figure 2.

due to the introduction of (i) the graphene layer and (ii) the change in the PI spacer thickness, in the structure, respectively; see Figure 2b. That is, the effective conductivity induced by the graphene layer situated in the near field of the FSS turns into $\alpha_1\sigma_{graphene}$ and the effective capacitance of the structure becomes $\alpha_2 C$. Since the overall structure thickness is much smaller than the THz wavelength, lumped elements can be employed to describe all the components of the structure. Using the R, L, and C values obtained in the first step, we are able to fit the measured THz transmission on our graphene/FSS hybrid samples by using the formula

$$T = \left| \frac{2}{2 + \alpha_1\sigma_{graphene}Z_0 + j\omega\alpha_2 CZ_0 + Z_0/(j\omega L + R)} \right|^2 \quad (3)$$

Here the only unknowns are α_1 and α_2, which could be obtained through fitting (solid lines) of the equation to experimental results (dots), as shown in Figure 4c and d. Each measured transmission spectrum produces a pair of α_1 and α_2, which are listed in Table 1 for samples with different graphene

Table 1. Extracted α_1 and α_2 by Fitting Measured Transmission with Eq 3 for Samples with Different PI Spacer Thicknesses and Graphene Conductivities

sample set #	d (μm)	σ_{dc} (mS)	α_1	α_2	notes
#1	16.5	0.73	7.078	0.971	nonpatterned
		1.32	7.061	0.971	
		1.98	6.850	0.953	
#2	9.4	0.65			nonpatterned, chemically doped
		0.81			
		1.10			
		1.96			
#3	16.5	0.80	7.092	0.971	nonpatterned
	9.4	0.81	10.607	0.794	
	4.5	0.78	15.694	0.684	
#4	16.5	0.84			patterned
		1.45			
		1.99			

conductivities and PI spacer thicknesses. As expected, while d is fixed, e.g., at 16.5 μm, the obtained values for α_1 and α_2 do not vary when altering the graphene conductivity. This can be noticed when analyzing the data extracted from sample set #1; in this case the transmission is altered by changing the number of graphene layers; however, because of their intrinsic physical meaning, i.e., α_1 being related to the field enhancement in the plane of graphene and α_2 to the effective permittivity defining the capacitor in the FSS equivalent circuit model, these two parameters (α_1 and α_2) will be affected only if changing the sample thickness and/or the graphene placement rather than when changing its conductivity. The fact that α_1 is ~7 for the samples with d = 16.5 μm indicates that the effective field in graphene is enhanced by $\alpha_1 \approx 7$ times due to a stronger light−matter interaction when graphene is placed close to the FSS. It could also be understood that $\alpha_2 \approx 1$ for sample set #1 because the value of C used here was also extracted on a sample with d = 16.5 μm in the first step (Figure 4b), leading thus to the same capacitance. In contrast, in terms of samples having different PI spacer thicknesses but the same graphene conductivity, e.g., when analyzing the data extracted from sample set #3, we observe that both α_1 and α_2 are changed. As graphene is placed closer to the FSS, α_1 increases from 7.092 (d = 16.5 μm) to 15.694 (d = 4.5 μm), which is caused by an even stronger light−matter interaction between the THz waves and graphene. At the same time, α_2 decreases because of a lower effective permittivity, thus equivalent capacitance, in thinner samples. In order to instructively determine the trends of α_1 and α_2 when varying d, we performed HFSS simulations by varying the graphene sheet conductivity and the PI spacer thickness, fitting the simulation results to the transmission line model (see Figure 5a,b), and extracting from there a series of values for α_1 and α_2. Applying the assumptions that $\alpha_1 = \exp(-c_1 d + c_2) + 1$ and $\alpha_2 = c_3 + c_4/\sqrt{(1 + c_5/d)}$, we can find values for the constants c_1 to c_5 (listed in Table 2) simply by fitting these to the extracted values of α_1 and α_2, as shown in Figure 5c,d. The particular functional dependence we employed for α_1 as a function of d was chosen by assuming α_1 proportional to the field enhancement in the plane of graphene, thus exponentially decaying over a distance with an asymptotic limit equal to 1.

DOI: 10.1021/acsphotonics.5b00639
ACS Photonics 2016, 3, 315−323

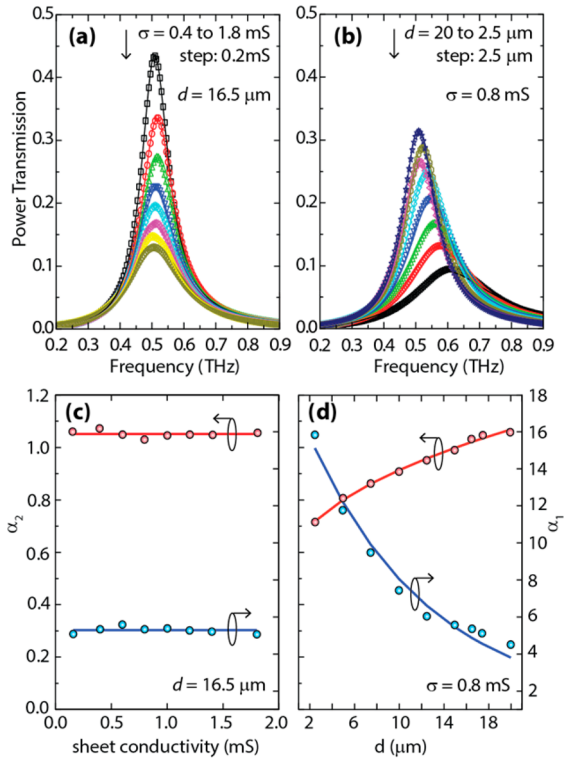

Figure 5. Simulated THz transmission spectra when changing the graphene sheet conductivity and PI spacer thickness. (a) Simulated (symbols) and fitted (solid lines) transmission spectra for a structure with d = 16.5 μm for different values of graphene conductivity. (b) Simulated (symbols) and fitted (solid lines) transmission spectra for a structure with σ_{DC} = 0.8 mS for different values of d. (c) Extracted α_1 and α_2 (symbols) versus sheet conductivity (for a structure with d = 16.5 μm); α_1 and α_2 are observed to be independent of the graphene conductivity in our simulations as well as in our experiments (see Table 1). (d) Extracted α_1 and α_2 (symbols) versus spacer thickness d (for a structure with σ_{DC} = 0.8 mS) and their fittings (solid lines); as d is increased, α_1 exponentially decays, whereas α_2 follows a nonlinear trend that physically arises from a larger effective permittivity in the structure.

Table 2. Fitted Constants c_1−c_5 Using Extracted Values for α_1 and α_2 from the Simulated THz Transmission Spectra in Various Cases[a]

	c_1	c_2	c_3	c_4	c_5
fitting to simulations	0.092	2.88	0.52	2.39	361.97

[a]The corresponding fitting curves and extracted α_1 and α_2 are shown in Figure 5c,d.

For α_2, the effective permittivity that sets the FSS equivalent circuit model capacitance (to which α_2 is proportional to) should have a similar dependence to that of the effective permittivity in a coplanar waveguide.[42] From Figure 5d, it could be seen that both α_1 and α_2 can be fitted well with the suggested relations as a function of distance d. Because our experimentally explored values for d cover a reasonably wide range (4.5−16.5 μm), the model parameter estimations we provide here are practical and instructive. To this end, we are able to evaluate the MD and IL for a given d and a conductivity swing range of the active material (graphene in this work), via employing compact mathematical formulas rather than time-consuming full wave electromagnetic simulations.

In Figure 6, we compute the expected performance for our graphene/FSS hybrid modulator design. The red dots (solid)

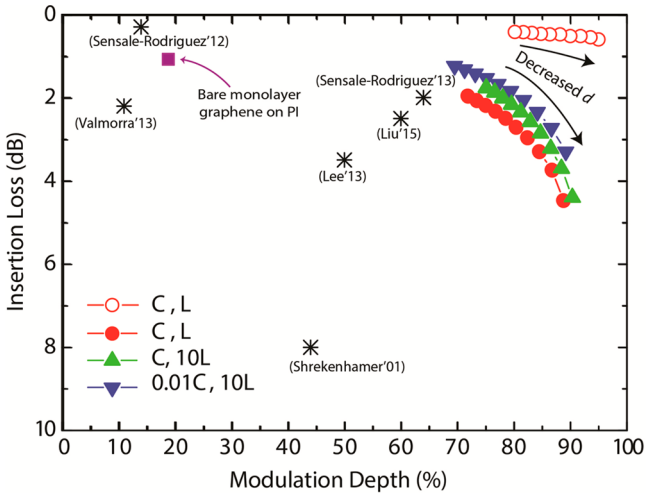

Figure 6. Modulation depth versus insertion loss for the THz modulator designs analyzed in this work. Three types of solid markers, respectively, show the modeled modulation depth and insertion loss using different values of C and L, while d changes from 1.5 to 16 μm. The solid symbols represent MD and IL, while sheet conductivity σ swings from 0.15 to 1 mS and red hollow symbols indicate MD and IL with σ changes from 0 to 1 mS. Both modulation depth and insertion loss values are taken at the resonance frequency, which is shifted as the product of C and L is varied. We also calculated the performance of the modulator if employing a pair of self-gated 2D semiconductors with a finite band gap[20] (for example, black phosphorus, MoS_2) by assuming a conductivity swing of 0−1 mS (hollow, red circles). Besides, the state-of-the-art performance of THz modulators reported in the literature is also plotted as stars in the figure.

show the calculated MD and IL when the graphene sheet conductivity is varied from 0.15 to 1 mS (a typical conductivity range for large-area CVD graphene) for a series of values of d (ranging from 1 to 16.5 μm) using the values of R, L, C, and the constants c_1−c_5 extracted as described above. In this figure, the optimal designs in terms of MD versus IL trade-off will be the ones closest to the upper right corner, which correspond to a d of around 7 μm, which is particularly suitable for the metamaterial structure we analyzed here. Other than that, green and blue triangles represent calculated performances if C and L are changed from our extracted values. It can be seen that high L and lower C are desirable in order to achieve better performance, which can be realized by optimizing the geometry of the metallic FSS. We want to emphasize that the particular relations (i.e., values of the extracted constants c_1−c_5) of d versus α_1 and α_2 obtained here specifically work for the employed FSS geometry depicted in Figure 1; however, the scaling trends of these parameters with d will hold for any other FSS design. From these observations, to fully make use of the proposed design method in order to provide designs achieving even more superior performance, future work on optimizing the FSS geometry is required. One of the advantages of utilizing the TLM method proposed here is that, as long as a few data points of T as a function d and $\sigma_{graphene}$ are obtained by experiments (or time-consuming numerical simulations), it is possible to estimate the performance of the device in terms of its MD and IL efficiently by means of a compact mathematical formula. Finally, it is worth mentioning that the sheet

DOI: 10.1021/acsphotonics.5b00639
ACS Photonics 2016, 3, 315−323

conductivity of the CVD-grown graphene layers we used in this work is relatively high, leading to a low transmission in our measurements. From Figure 3b, it is expected that THz transmission may reach as much as 60% if the minimum graphene sheet conductivity could be reduced to 0.15 mS when using d = 16.5 μm as a spacer thickness. If a pair of self-gated 2D semiconductors with a finite band gap[20] (for example, black phosphorus, MoS_2) is employed as the active material instead of graphene, we can expect the lowest conductivity of the active material can be tuned to be near zero. This leads to a near-zero insertion loss, thus approaching the ideal modulator performance: less than 0.5 dB IL with more than 90% MD (the hollow red circles in Figure 6; by assuming a conductivity swing of 0−1 mS). Besides, we plot state-of-the-art performance of THz modulators reported in the literature,[22,23,25,26,37,43] and it could be seen that our modulator design predicts great potential to realize high-performance THz modulators using the proposed device structure.

CONCLUSIONS

In conclusion, by integrating both two-dimensional graphene and metallic surfaces into a three-dimensional structure, we demonstrate that light−matter interaction can be considerably enhanced due to the ability of confining THz waves into a small volume by the FSS. It is experimentally shown that such enhancement could be tuned by means of placing the graphene layers at various separations from the FSS, which is extremely useful for extending such a hybrid stack device concept to other active material systems rather than graphene in the THz range or even to other frequency regimes. A simple TLM method was developed to explain and predict the behavior of hybrid THz modulator devices, exhibiting good agreement with experiments. Our results indicate that, due to the presence of the FSS, the active area required for modulation is reduced to just the region complementary to the FSS, thus leading to improved operation speed, which is limited by the *RC* constant of the device. In summary, from all these points of view, the discussion presented in this work suggests that the addition of passive FSS in graphene-based THz modulators and the optimization of the geometrical parameters in these structures can allow simultaneously realizing high MD, low IL, and fast operation. Due to its broad design flexibility, the proposed design strategies could also be readily generalized into other material systems, device geometries, or frequency ranges.

ASSOCIATED CONTENT

Supporting Information

The Supporting Information is available free of charge on the ACS Publications website at DOI: 10.1021/acsphotonics.5b00639.

The THz transmission spectra for graphene layers on a bare PI substrate, which were used to extract the graphene conductivity and the effect of carrier lifetime on the performance of the analyzed hybrid structure (PDF)

AUTHOR INFORMATION

Corresponding Authors

*E-mail (R. Yan): ry253@cornell.edu.
*E-mail (B. Sensale-Rodriguez): berardi.sensale@utah.edu.
*E-mail (H. G. Xing): grace.xing@cornell.edu.

Notes

The authors declare no competing financial interest.

ACKNOWLEDGMENTS

The authors acknowledge the support from NSF (ECCS-1202452 and CAREER 0846910). B.S.-R. acknowledges the support from the NSF MRSEC program at the University of Utah under grant no. DMR 1121252 and from the NSF CAREER award no. 1351389. The device fabrication was performed at Notre Dame Nanofabrication (NDNF) facility.

REFERENCES

(1) Geim, A. K.; Novoselov, K. S. The Rise of Graphene. *Nat. Mater.* **2007**, *6*, 183−191.
(2) Novoselov, K. S.; Geim, A. K.; Morozov, S. V.; Jiang, D.; Katsnelson, M. I.; Grigorieva, I. V.; Dubonos, S. V.; Firsov, A. A. Two-Dimensional Gas of Massless Dirac Fermions in Graphene. *Nature* **2005**, *438*, 197−200.
(3) Mueller, T.; Xia, F.; Avouris, P. Graphene Photodetectors for High-Speed Optical Communications. *Nat. Photonics* **2010**, *4*, 297−301.
(4) Yan, R.; Zhang, Q.; Li, W.; Calizo, I.; Shen, T.; Richter, C. a.; Hight-Walker, A. R.; Liang, X.; Seabaugh, A.; Jena, D.; Grace Xing, H.; Gundlach, D. J.; Nguyen, N. V. Determination of Graphene Work Function and Graphene-Insulator-Semiconductor Band Alignment by Internal Photoemission Spectroscopy. *Appl. Phys. Lett.* **2012**, *101*, 022105.
(5) Li, X.; Cai, W.; An, J.; Kim, S.; Nah, J.; Yang, D.; Piner, R.; Velamakanni, A.; Jung, I.; Tutuc, E.; Banerjee, S. K.; Colombo, L.; Ruoff, R. S. Large-Area Synthesis of High-Quality and Uniform Graphene Films on Copper Foils. *Science* **2009**, *324*, 1312−1314.
(6) Nicolosi, V.; Chhowalla, M.; Kanatzidis, M. G.; Strano, M. S.; Coleman, J. N. Liquid Exfoliation of Layered Materials. *Science* **2013**, *340*, 1226419.
(7) Paton, K. R.; Varrla, E.; Backes, C.; Smith, R. J.; Khan, U.; O'Neill, A.; Boland, C.; Lotya, M.; Istrate, O. M.; King, P.; Higgins, T.; Barwich, S.; May, P.; Puczkarski, P.; Ahmed, I.; Moebius, M.; Pettersson, H.; Long, E.; Coelho, J.; O'Brien, S. E.; McGuire, E. K.; Sanchez, B. M.; Duesberg, G. S.; McEvoy, N.; Pennycook, T. J.; Downing, C.; Crossley, A.; Nicolosi, V.; Coleman, J. N. Scalable Production of Large Quantities of Defect-Free Few-Layer Graphene by Shear Exfoliation in Liquids. *Nat. Mater.* **2014**, *13*, 624−630.
(8) Cohen-Tanugi, D.; Grossman, J. C. Water Desalination across Nanoporous Graphene. *Nano Lett.* **2012**, *12*, 3602−3608.
(9) Liu, C.; Yu, Z.; Neff, D.; Zhamu, A.; Jang, B. Z. Graphene-Based Supercapacitor with an Ultrahigh Energy Density. *Nano Lett.* **2010**, *10*, 4863−4868.
(10) Min, S. K.; Kim, W. Y.; Cho, Y.; Kim, K. S. Fast DNA Sequencing with a Graphene-Based Nanochannel Device. *Nat. Nanotechnol.* **2011**, *6*, 162−165.
(11) Sensale-Rodriguez, B.; Yan, R.; Liu, L.; Jena, D.; Xing, H. G. Graphene for Reconfigurable Terahertz Optoelectronics. *Proc. IEEE* **2013**, *101*, 1705−1716.
(12) Otsuji, T.; Member, S.; Watanabe, T.; Tombet, S. A. B.; Satou, A.; Knap, W. M.; Popov, V. V.; Ryzhii, M.; Ryzhii, V. *IEEE Trans. Terahertz Sci. Technol.* **2013**, *3*, 63−71.
(13) Vicarelli, L.; Vitiello, M. S.; Coquillat, D.; Lombardo, A.; Ferrari, A. C.; Knap, W.; Polini, M.; Pellegrini, V.; Tredicucci, A. Graphene Field-Effect Transistors as Room-Temperature Terahertz Detectors. *Nat. Mater.* **2012**, *11*, 865−871.
(14) Tonouchi, M. *Nat. Photonics* **2002**, *1*, 97−105.
(15) Kleine-Ostmann, T.; Dawson, P.; Pierz, K.; Hein, G.; Koch, M. Room-Temperature Operation of an Electrically Driven Terahertz Modulator. *Appl. Phys. Lett.* **2004**, *84*, 3555−3557.
(16) Chen, H.-T.; Padilla, W. J.; Zide, J. M. O.; Gossard, A. C.; Taylor, A. J.; Averitt, R. D. Active Terahertz Metamaterial Devices. *Nature* **2006**, *444*, 597−600.
(17) Han, J.; Lakhtakia, A. Semiconductor Split-Ring Resonators for Thermally Tunable Terahertz Metamaterials. *J. Mod. Opt.* **2009**, *56*, 554−557.

DOI: 10.1021/acsphotonics.5b00639
ACS Photonics 2016, 3, 315−323

(18) Golosovsky, M.; Neve-Oz, Y.; Davidov, D. Magnetic-Field-Tunable Photonic Stop Band in a Three-Dimensional Array of Conducting Spheres. *Phys. Rev. B: Condens. Matter Mater. Phys.* **2005**, *71*, 195105.
(19) Rahm, M.; Li, J.-S.; Padilla, W. THz Wave Modulators: A Brief Review on Different Modulation Techniques. *J. Infrared, Millimeter, Terahertz Waves* **2013**, *34*, 1−27.
(20) Yan, R.; Sensale-Rodriguez, B.; Liu, L.; Jena, D.; Xing, H. G. A New Class of Electrically Tunable Metamaterial Terahertz Modulators. *Opt. Express* **2012**, *20*, 28664−28671.
(21) Degl'innocenti, R.; Jessop, D. S.; Shah, Y. D.; Sibik, J.; Zeitler, A.; Kidambi, P. R.; Hofmann, S.; Beere, H. E.; Ritchie, D. a. Low-Bias Terahertz Amplitude Modulator Based on Split-Ring Resonators and Graphene. *ACS Nano* **2014**, *8*, 2548−2554.
(22) Valmorra, F.; Scalari, G.; Maissen, C.; Fu, W.; Schönenberger, C.; Choi, J. W.; Park, H. G.; Beck, M.; Faist, J.; Scho, C. Low-Bias Active Control of Terahertz Waves by Coupling Large-Area CVD Graphene to a Terahertz Metamaterial. *Nano Lett.* **2013**, *13*, 3193−3198.
(23) Liu, P. Q.; Luxmoore, I. J.; Mikhailov, S. A.; Savostianova, N. a; Valmorra, F.; Faist, J.; Nash, G. R. *Highly Tunable Hybrid Metamaterials Employing Split-Ring Resonators Strongly Coupled to Graphene Surface Plasmons. arXiv1501.05490.*
(24) Wu, Y.; La-o-vorakiat, C.; Qiu, X.; Liu, J.; Deorani, P.; Banerjee, K.; Son, J.; Chen, Y.; Chia, E. E. M.; Yang, H. Graphene Terahertz Modulators by Ionic Liquid Gating. *Adv. Mater.* **2015**, *27*, 1874−1879.
(25) Sensale-Rodriguez, B.; Yan, R.; Kelly, M. M.; Fang, T.; Tahy, K.; Hwang, W. S.; Jena, D.; Liu, L.; Xing, H. G. Broadband Graphene Terahertz Modulators Enabled by Intraband Transitions. *Nat. Commun.* **2012**, *3*, 780.
(26) Sensale-Rodriguez, B.; Yan, R.; Rafique, S.; Zhu, M.; Li, W.; Liang, X.; Gundlach, D.; Protasenko, V.; Kelly, M. M.; Jena, D.; Liu, L.; Xing, H. G. Extraordinary Control of Terahertz Beam Reflectance in Graphene Electro-Absorption Modulators. *Nano Lett.* **2012**, *12*, 4518−4522.
(27) Sensale-Rodriguez, B.; Fang, T.; Yan, R.; Kelly, M. M.; Jena, D.; Liu, L.; Xing, H. G. Unique Prospects for Graphene-Based Terahertz Modulators. *Appl. Phys. Lett.* **2011**, *99*, 113104.
(28) Park, H. R.; Namgung, S.; Chen, X.; Lindquist, N. C.; Giannini, V.; Francescato, Y.; Maier, S. A.; Oh, S. H. Perfect Extinction of Terahertz Waves in Monolayer Graphene over 2-nm-Wide Metallic Apertures. *Adv. Opt. Mater.* **2015**, *3*, 667−673.
(29) Yan, H.; Li, X.; Chandra, B.; Tulevski, G.; Wu, Y.; Freitag, M.; Zhu, W.; Avouris, P.; Xia, F. Tunable Infrared Plasmonic Devices Using Graphene/insulator Stacks. *Nat. Nanotechnol.* **2012**, *7*, 330−334.
(30) Yan, H.; Xia, F.; Zhu, W.; Freitag, M.; Dimitrakopoulos, C.; Bol, A. a; Tulevski, G.; Avouris, P. Infrared Spectroscopy of Wafer-Scale Graphene. *ACS Nano* **2011**, *5*, 9854−9860.
(31) Porterfield, D. W.; Hesler, J. L.; Densing, R.; Mueller, E. R.; Crowe, T. W.; Weikle, R. M., II. Resonant Metal-Mesh Bandpass Filters for the Far Infrared. *Appl. Opt.* **1994**, *33*, 6046−6052.
(32) Choi, H. K.; Lee, S. H. S.; Choi, C.; Choi, S.-Y.; Zhang, X.; Choi, M.; Kim, T.-T.; Liu, M.; Yin, X.; Min, B. Switching Terahertz Waves with Gate-Controlled Active Graphene Metamaterials. *Nat. Mater.* **2012**, *11*, 936−941.
(33) Bae, S.; Kim, H.; Lee, Y.; Xu, X.; Park, J.-S.; Zheng, Y.; Balakrishnan, J.; Lei, T.; Kim, H. R.; Song, Y. I.; Kim, Y.-J.; Kim, K. S.; Ozyilmaz, B.; Ahn, J.-H.; Hong, B. H.; Iijima, S. Roll-to-Roll Production of 30-Inch Graphene Films for Transparent Electrodes. *Nat. Nanotechnol.* **2010**, *5*, 574−578.
(34) Shin, D.-W.; Lee, J. H.; Kim, Y.-H.; Yu, S. M.; Park, S.-Y.; Yoo, J.-B. A Role of HNO3 on Transparent Conducting Film with Single-Walled Carbon Nanotubes. *Nanotechnology* **2009**, *20*, 475703.
(35) Sensale-Rodriguez, B.; Yan, R.; Rafique, S.; Zhu, M.; Kelly, M.; Protasenko, V.; Jena, D.; Liu, L.; Xing, H. G. Exceptional Tunability of THz Reflectance in Graphene Structures. In *2012 37th International Conference on Infrared, Millimeter, and Terahertz Waves (IRMMW-THz)*; IEEE, 2012; pp 1−3.
(36) Gao, W.; Shu, J.; Reichel, K.; Nickel, D. V.; He, X.; Shi, G.; Vajtai, R.; Ajayan, P. M.; Kono, J.; Mittleman, D. M.; Xu, Q. High-Contrast Terahertz Wave Modulation by Gated Graphene Enhanced by Extraordinary Transmission through Ring Apertures. *Nano Lett.* **2014**, *14*, 1242−1248.
(37) Lee, S. H.; Kim, H.; Choi, H. J.; Kang, B.; Cho, Y. R.; Min, B. Broadband Modulation of Terahertz Waves With Non-Resonant Graphene Meta-Devices. *IEEE Trans. Terahertz Sci. Technol.* **2013**, *3*, 764−771.
(38) Weis, P.; Garcia-Pomar, J. L.; Höh, M.; Reinhard, B.; Brodyanski, A.; Rahm, M. Spectrally Wide-Band Terahertz Wave Modulator Based on Optically Tuned Graphene. *ACS Nano* **2012**, *6*, 9118−9124.
(39) Leong, W. S.; Gong, H.; Thong, J. T. Low-contact-resistance Graphene devices with Nickel-etched-Graphene contacts. *ACS Nano* **2013**, *8*, 994−1001.
(40) Pozar, D. M. *Microwave Engineering*; John Wiley & Sons, 2009.
(41) Yao, Y.; Kats, M. A.; Genevet, P.; Yu, N.; Song, Y.; Kong, J.; Capasso, F. Broad Electrical Tuning of Graphene-Loaded Plasmonic Antennas. *Nano Lett.* **2013**, *13*, 1257−1264.
(42) Jha, A. R. *Mems and Nanotechnology-Based Sensors and Devices for Communications, Medical and Aerospace Applications*; CRC Press, 2008.
(43) Shrekenhamer, D.; Rout, S.; Strikwerda, A. C.; Bingham, C.; Averitt, R. D.; Sonkusale, S.; Padilla, W. J. High speed terahertz modulation from metamaterials with embedded high electron mobility transistors. *Opt. Express* **2011**, *19*, 9968−9975.

DOI: 10.1021/acsphotonics.5b00639
ACS Photonics 2016, 3, 315−323